How Criticality Meets Bifurcation in Compressive Failure of Disordered Solids

Ashwij Mayya, Estelle Berthier, and Laurent Ponson*
Institut Jean Le Rond D'Alembert UMR 7190, Sorbonne Université, CNRS, Paris, France

(Received 12 November 2022; revised 10 April 2023; accepted 15 August 2023; published 25 October 2023)

Continuum mechanics describes compressive failure as a standard bifurcation in the response of a material to an increasing load: Damage, which initially grows uniformly in the material, localizes within a thin band at failure. Yet, experiments recording the acoustic activity preceding localization evidence power-law-distributed failure precursors of increasing size, suggesting that compressive failure is a critical phenomenon. We examine here this apparent contradiction by probing the spatial organization of the damage activity and its evolution until localization during compression experiments of 2D cellular solids. The intermittent damage evolution measured in our experiments is adequately described by a nonstationary depinning equation derived from damage mechanics and reminiscent of critical phenomena. In this description, precursors are damage cascades emerging from the interplay between the material's disorder and the long-range stress redistributions following individual damage events. Yet, the divergence of their characteristic size close to failure, which we observe in our experiments, is not the signature of a transition toward criticality. Instead, the system remains at a fixed distance to the critical point at all stages of the damage evolution. The divergence results from the progressive loss of stability of the material as it is driven toward localization. Thus, our study shows that compressive failure is a standard bifurcation for which the material disorder plays a marginal role. It also implies that the precursory acoustic activity behaves as a tracer of the evolution of materials toward failure and can therefore be used to assess their residual lifetime.

DOI: 10.1103/PhysRevX.13.041014

Subject Areas: Mechanics, Soft Matter, Statistical Physics

I. INTRODUCTION

Damage localization is the standard mode of failure of materials under compression. Decoding this degradation process is therefore the cornerstone of the design of reliable and safe structures such as buildings, bridges, tunnels, and a countless number of mechanical parts under compressive loading conditions. During their life in service, these structures may progressively lose their mechanical integrity. Comprehending damage evolution to predict their remaining lifetime is an essential component of modern tools of structural design and predictive maintenance. Yet, the appropriate theoretical concepts for describing damage spreading and ultimately localization are still vigorously debated and constitute an active topic of research [1–4].

Continuum damage mechanics is a powerful approach for describing the compressive failure of materials such as rocks, ceramics, or mortar [5–8]. In this framework, discrete damage mechanisms like microcrack growth are described at a continuum scale through the degradation of the local elastic stiffness of the material [9–15]. Beyond some critical load level, this softening leads to a bifurcation from the homogeneous damage field to a localized damage that grows only within a thin band and leads to material failure [16,17].

In parallel, and almost independent of the development of damage mechanics, the intermittent dynamics of damage growth preceding compressive failure has attracted a lot of attention. Acoustic emissions have been used as a preferential means of experimental investigation. Experimental measurements reveal that damage grows through bursts that display robust scale-free statistics [6,11,18–26]. Accounting for material disorder, various theoretical works [27–31] have proposed to describe failure as a discontinuous (first-order) phase transition where the precursory damage events emerge from the sweeping of an instability. These ideas were primarily discussed in the context of toy models of failure, using, e.g., random fuse models. As a result, a direct comparison with the statistical properties of precursors measured experimentally was not possible, leaving unresolved the applicability of these concepts to real materials. Motivated by the observation of an increase of the precursors' size close to localization [23,26,32–35], an alternative scenario in which compressive failure is described as a continuous (second-order)

*laurent.ponson@sorbonne-universite.fr

phase transition was also proposed [26,33,36–41]: Similar to a large range of driven disordered elastic systems [42–44], the bursts of activity characterizing the response of damaging materials was interpreted as critical fluctuations, or avalanches, that are reminiscent of the so-called depinning transition, a critical phenomenon emerging from the competition between disorder and elastic interactions. Above a depinning threshold, damage is thus expected to grow at some finite speed, eventually leading to failure. When approaching this critical point, the material should then display scale-free fluctuations with diverging length and timescales, a feature that has been observed in some compression experiments [26,41].

Despite the appeal of such a scenario, it comes in direct contradiction with continuum damage models which describe compressive failure as a standard bifurcation taking place in homogeneous solids, for which material disorder and hence precursors play a minor role. The objective of this work is to reconcile these two seemingly incompatible scenarios: Is compressive failure a standard bifurcation or a depinning transition? Are its precursors the result of a transition toward a critical point? These interrogations have crucial engineering implications: Do precursory damage events foretell impending failure? Recently, we examined this issue in a 1D toy model [45]. However, the generalization of our results to real materials was limited by the short-range interactions and the system dimension considered in our model. Here, we follow a different approach: We start from the in-depth characterization of the damage precursors in a model experimental system. Subsequently, experimental observations are confronted with the competing scenarios, yielding our two main results:

(i) The scale-free statistics of the precursory activity is reminiscent of the avalanche dynamics during depinning of a driven disordered elastic interface. Yet, in stark contrast with the critical transition scenario, the divergence of the length and the timescales of precursors close to failure results from the oncoming localization, a standard bifurcation taking place in homogeneous solids.

(ii) This approach toward bifurcation does not drive the damaging solid toward a critical point. Instead, it remains at some finite distance from criticality during the whole process of damage accumulation.

Our article is structured as follows. First, we present our experimental setup (Sec. II). We carry out a compression test of cohesionless soft cellular solids. We show that this material behaves like an elastodamageable medium, ensuring the applicability of our findings to other brittle materials. The characteristic features of the precursory damage activity are then analyzed at both the global scale (using the force-displacement response of the specimen) and the local scale (using full-field measurements of the mechanical quantities). This multiscale characterization provides the complete (nonstationary) statistical structure of precursors that follows robust scaling laws. To rationalize these experimental observations, we use damage mechanics that we extend to disordered solids (Sec. III). We derive the evolution equation of the damage field that reveals the complex connection with driven disordered elastic interfaces and depinning transition. Our approach also captures damage localization that is described as a standard instability. In Sec. IV, we come back to our experimental data and validate several nonstandard aspects of the proposed depinning model. The compatibility of both competing scenarios with our experimental observations is discussed in Sec. V. We argue that damage spreading is reminiscent of the nonstationary depinning dynamics of a driven disordered elastic interface that culminates in a standard bifurcation at localization. Section VI provides a direct engineering application of our work. We bring the experimental proof of concept that precursors can be harnessed for predicting the residual lifetime of structures. The analysis of the acoustic emissions recorded during our experiments is presented in Sec. VII. Their statistical similarity to the acoustic precursors recorded during the failure of standard brittle solids ensures the generality of our results. The numerical resolution of the proposed damage model is carried out in Sec. VIII. It provides a comprehensive interpretation of the statistics of failure precursors observed in our experiments. Finally, the broader implications of the proposed nonstationary depinning scenario of other phenomena including amorphous plasticity are discussed in Sec. IX. The methods employed in our experiments and our model are briefly presented in Appendixes A and B. A thorough description is provided in the Supplemental Material [46].

II. EXPERIMENTAL INVESTIGATION OF FAILURE PRECURSORS

A. Damage localization

Taking inspiration from Poirier *et al.*'s experiments [47], we perform compression tests of 2D cohesionless soft cellular solids as shown in Fig. 1(a). The results presented below are based on ten different experiments during which the evolution of the material microstructure and the associated damage is tracked using full-field measurements (see Appendix A 1 for a detailed description of our experimental setup). Following Karimi *et al.* [48], the effect of friction between cells is described at a mesoscopic continuum scale by introducing an equivalent elastodamageable medium. As shown in the following sections and justified in detail in Appendix A 2, such a cohesionless cellular solid is a model system that mimics the jerky dissipative response of brittle disordered solids under compression. Dissipation taking place at the scale of the individual cells is tracked in space and time using a high-speed camera (see Appendixes A 4 and A 5 and Supplemental Material [46] Secs. 1 and 2 for details). We thus circumvent the drawbacks inherent to x-ray

tomography that provides the detailed spatial structure of damage events in 3D materials but at the cost of temporal resolution [49,50]. We also overcome the limitations of acoustic emissions that provide highly resolved time series but with a rather poor spatial resolution [51,52].

First, we focus on the average mechanical response of the specimen. A typical force-displacement curve recorded during a compression test under displacement control conditions is shown in Fig. 1(b). As evidenced from the snapshots of the experiments taken at different load levels [top inset of Fig. 1(b) and Supplemental Material Video S1 [46]], the specimen initially deforms rather uniformly, even beyond the linear elastic regime. We consider the deviation to cell circularity beyond the elastic limit as a measure of the damage level, $d_\circ$. As shown in the inset of Fig. 1(c), the larger the $d_\circ$, the lower the Young's modulus $E(d_\circ)$ of the material, as expected for elastodamageable media. Together with its Poisson ratio $\nu(d_\circ) \simeq \nu_\circ$ that remains nearly constant, the function $E(d_\circ)$ describes the impact of damage on the mechanical response of our 2D elastodamageable solid (see Appendix A 2). Damage is observed to grow homogeneously from the elastic limit $F = F_{\rm el}$ until the peak load $F = F_{\rm c}$ (refer to Supplemental Material Table S1 [46] for a list of notations), except for the cells close to the boundary where friction with the lateral wall prevails. Tracking the collapsing of cells from their deviation to circularity $d_\circ > 0.5$, we observe that at peak load, no cell has collapsed yet, except at the boundaries. After peak load, however, a band consisting of progressively collapsing cells appears, initiating from the top corners of the structure. The localization band is clearly visible farther away from peak load, as shown on the snapshot in the upper right corner of Fig. 1(b). The onset loading $\Delta_{\rm c}$ of localization is inferred from the evolution of the vertical strain $\langle \epsilon_{yy} \rangle_{\mathcal{R}_2}$ averaged over the bottom region $\mathcal{R}_2$ of the specimen [indicated in Fig. 1(a)]: As displayed in the lower inset of Fig. 1(b), for $\Delta > \Delta_{\rm c}$, $\langle \epsilon_{yy} \rangle_{\mathcal{R}_2}$ saturates and departs from the strain $\epsilon_{yy}^{\rm ext}$ imposed by the loading machine. On the contrary, the strain $\langle \epsilon_{yy} \rangle_{\mathcal{R}_1}$ measured in the upper region $\mathcal{R}_1$ follows the imposed strain. This confirms that damage localization starts at peak load. To confirm this important result, we investigate the spatial distribution of the damage growth rate near peak load (see Appendix A 5). Before peak load, it is rather homogeneously distributed, while right after peak load, its value is several times larger in the thin band where cells start to progressively collapse.

This behavior is consistent with the observations made in a wide range of brittle solids [51,53–56]. It is also captured by the nonlocal damage models recently proposed in Berthier *et al.* [57] and Dansereau *et al.* [58] (see Supplemental Material Sec. S3F [46] for the analytical prediction). If the experiments were under force-control conditions, as in most real-life structural applications, a sudden collapse of the cells resulting in the catastrophic failure of the specimen would also occur at peak load.

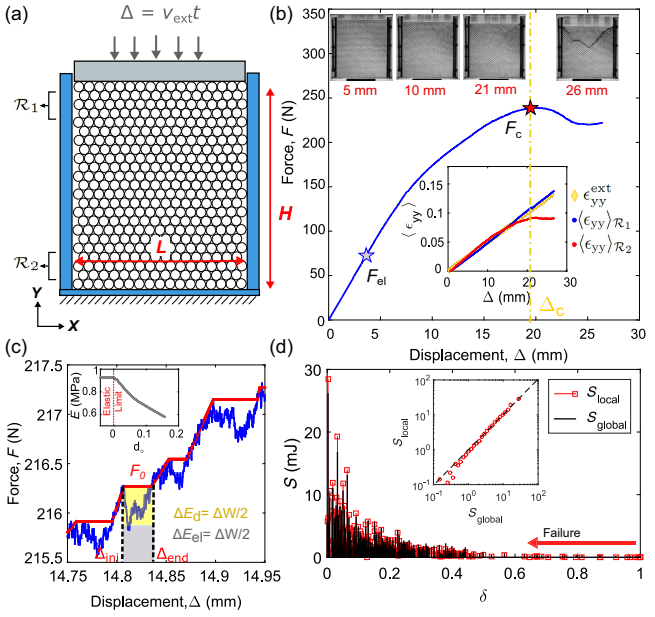

FIG. 1. (a) Schematic of the compression experiment depicting the front view of the hexagonal packing of soft cellular solids. The box dimensions are $205 \times 170 \times 30$ mm^3. Owing to the displacement Δ applied to the specimen through a piston moving at a rate $v_{\rm ext}$, the cells undergo a deformation that is recorded using a high-speed camera. The following figures describe the typical mechanical response of the specimens, as observed in one of our experiments. (b) Force-displacement response of the specimen. Top insets: The emergence of a localization band of collapsed cells corresponding to highly localized deformations is visible on the snapshots of the specimen taken at different load levels. Bottom inset: The strain level averaged over the bottom region $\mathcal{R}_2$ indicated in panel (a) saturates after localization for $\Delta > \Delta_{\rm c}$, while the one measured in the upper region $\mathcal{R}_1$ follows the linear trend $\epsilon_{yy}^{\rm ext} = \Delta/H = v_{\rm ext}t/L$ imposed by the loading machine. (c) Construction of an equivalent-force-control experiment from the mechanical response of the specimen measured under displacement control. The start and end of a damage precursor taking place at a constant force F_0 are denoted by $\Delta_{\rm ini}$ and $\Delta_{\rm end}$. The precursor size $S_{\rm global} = \Delta E_{\rm d}$ defined as the dissipated energy during the event corresponds to half the work of the external force $\Delta W = F_0(\Delta_{\rm end} - \Delta_{\rm ini})$. Inset: The stiffness degradation of the effective medium with increasing damage. (d) Variations of the precursor size S, in terms of dissipated energy, with the distance to failure δ. Inset: A comparison of precursor sizes computed from the global analysis and the local analysis.

B. Precursors as cascades of damage events

We now analyze the precursory damage activity taking place before peak load. A closer examination of the force-displacement curve in Fig. 1(c) reveals sudden force drops of amplitude much larger than the precision ± 0.05 N of our load cell. These drops are followed by a linear increase of the force, recovering the force drop albeit with a degraded macroscopic stiffness (lower slope). The investigation of the specimen response under different

loading rates shows similar behaviors. This alternating sequence of damage growth and elastic reloading is reminiscent of the avalanche dynamics observed in driven disordered elastic systems [42–44]. We construct the mechanical response of the specimen (in red) in an equivalent-force-control experiment where displacement jumps (from Δ_{ini} to Δ_{end}) at constant force corresponding to a cascade of damage growth, also called an avalanche [Fig. 1(c)]. The precursors defined this way can be shown to be statistically similar to those that would be measured during an actual force-control experiment (see Supplemental Material, Sec. S4 [46] for a numerical validation). As under force-control conditions, damage cascades take place at constant force, and the work of the loading machine ΔW during the event can be shown to contribute equally to the increase ΔE_{el} of the elastic energy and to the dissipation ΔE_{d} by damage (see Appendix A 3). Hence, $\Delta E_{\mathrm{d}} = \Delta W/2 = (\Delta_{\mathrm{end}} - \Delta_{\mathrm{ini}})F_0/2$, and we define this quantity as the precursor size S_{global}. The evolution of S_{global} with the distance to failure $\delta = (F_{\mathrm{c}} - F)/(F_{\mathrm{c}} - F_{\mathrm{el}})$ is shown in Fig. 1(d). The introduction of F_{el} ensures that $\delta = 1$ corresponds to the beginning of the damage accumulation regime. However, choosing another definition, as e.g., $(F_{\mathrm{c}} - F)/F_{\mathrm{c}}$, does not modify our conclusions. We note that the cascading dynamics and its amplification upon approaching failure ($\delta \to 0$) observed in our 2D cellular material under compression are reminiscent of the intermittent damage activity evidenced by acoustic emissions in standard brittle materials [see Fig. 1(d)].

Alternatively, we can also identify and characterize the precursors at the local scale using our (time-resolved) full-field measurement of the displacement and the damage field [see Supplemental Material Sec. 1C and Figs. S1(c)–S1(f) [46] for details on the local analysis]. From these quantities, we compute the field of stored elastic energy in the effective elastodamageable medium. Considering energy balance at the local scale, we can thus determine the dissipation energy density $\rho(\vec{x}, \Delta)$ that we integrate over an avalanche $\rho(\vec{x}) = \int_{\Delta_{\mathrm{ini}}}^{\Delta_{\mathrm{end}}} \rho(\vec{x}, \Delta) d\Delta$.

Maps of dissipation energy density $\rho(\vec{x})$ depicting the complex spatial structure of precursors are presented in Fig. 2(a). We observe a diffuse pattern, yet containing locally well-defined regions of varying intensity and size. These clusters are reminiscent of the time- and space-correlated structure of incremental damage events. In practice, highly correlated individual damage events can be grouped together by implementing a spatiotemporal clustering algorithm on the fields $\rho(\vec{x}, \Delta)$ recorded during $\Delta_{\mathrm{ini}} < \Delta < \Delta_{\mathrm{end}}$. This segmentation reveals the clusterlike structure of precursors illustrated in Fig. 2(b) (see also Video S2 in the Supplemental Material [46]) for the precursor shown in the second panel of Fig. 2(a).

The energy $S_{\mathrm{local}} = \int \rho(\vec{x}) d\vec{x}$ dissipated during the cascade compares well with the precursor size S_{global} inferred from the force-displacement response; see Fig. 1(d). It is also in good agreement with the precursor size computed using the field of dissipated energy inferred from the incremental damage field, thus validating the assumption of local energy balance [see Supplemental Material Sec. S2, Figs. S2(d) and S2(e) [46]]. Finally, this agreement supports the description of our cohesionless cellular solid as an elastodamageable medium.

C. Statistical characterization of precursors

We now explore the properties of the damage cascades observed in our experiments. First, their spatial extent is determined from (thresholded) maps of dissipation energy density [insets of Fig. 2(a)]. The employed threshold value ρ^* is inferred from the distribution of local dissipation densities that follows an exponential decay $P(\rho) \propto \mathrm{e}^{-\rho/\rho^*}$ [see Supplemental Material Sec. S1(c) and Fig. S1(g) [46]]. We extract the characteristic length ξ from the 2D autocorrelation of the thresholded dissipation map [Supplemental Material Sec. S1(d) and Fig. S1(h) [46]]. The length grows with the avalanche size as $S \propto \xi^{d_{\mathrm{f}}}$, where $d_{\mathrm{f}} \simeq 1.07$ is the fractal dimension; see Fig. 2(c). While cascades spread over the whole specimen [see Fig. 2(a)], ξ represents the spatial extent of the largest clusters constituting the cascade. Interestingly, ξ reaches the specimen size L upon approaching failure, which implies an upper limit on the size of the precursors. An independent estimate of the fractal dimension of the precursors is obtained from the spatial distributions of the clusters. We identify the location of their center of mass, as illustrated on the right end of Fig. 2(b), and then compute the correlation function $C(r) \propto r^{d_{\mathrm{f}}}$ defined as the fraction of pairs of points whose separation is less than r [59]. This provides a fractal dimension $d_{\mathrm{f}} \simeq 1.15$ [see inset of Fig. 2(c)] compatible with the one obtained from the spatial distribution of the individual damage events. Note that the spatial extent ξ of a damage cascade is different from its size S that corresponds to the energy dissipated by damage during the cascade.

We now seek to determine the characteristic duration of damage cascades. We come back to the force-displacement response and explore the sequence of load drops observed within an avalanche. The precursor duration T is defined as the number of load drops [also see Supplemental Material Sec. S1B and Figs. S1(a) and S1(b) [46]]. It scales with the characteristic length ξ of the precursor as $T \propto \xi^z$ [see Fig. 2(d)] with dynamic exponent $z \simeq 0.53$.

Thus, a damage cascade is characterized by its size, its spatial extent, and its duration. All three quantities are related to each other by scaling laws. The probability distribution of these quantities is studied in Fig. 2(e), where we focus on the distribution $P(S)$ of precursor sizes, the other distributions $P(\xi)$ and $P(T)$ being inferred from the previous scaling laws. Considering all the precursors ($\delta \in [0, 1]$) or only the ones close to localization ($\delta \in [0, 0.01]$), both distributions follow a power-law statistics but with two different exponents $\beta_{\mathrm{tot}} \simeq 2.34$ and

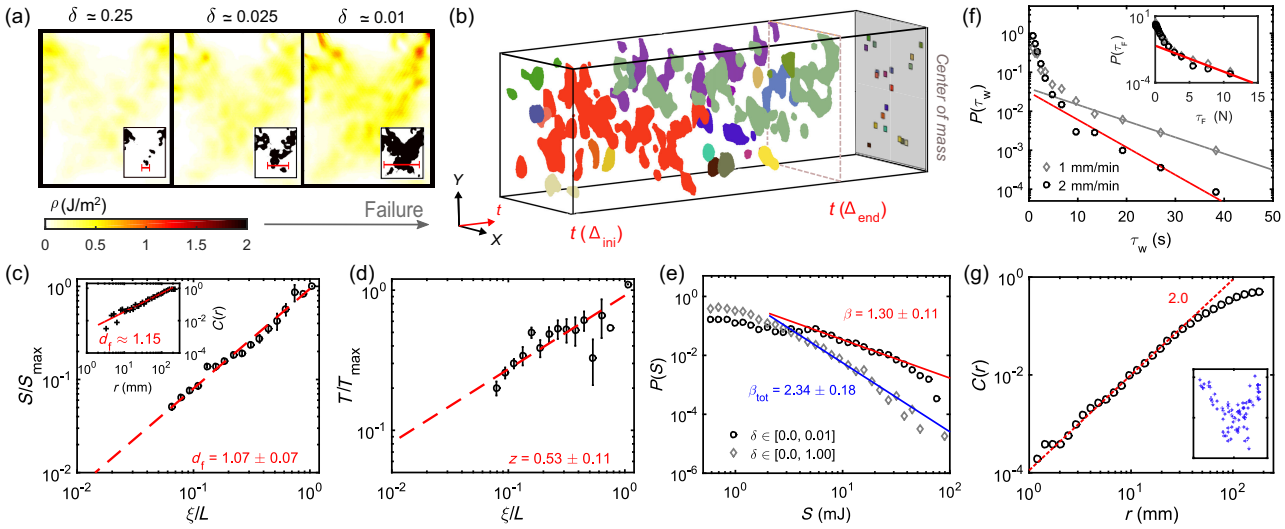

FIG. 2. (a) Energy density maps $\rho(\vec{x})$ and their corresponding binary thresholded formats (inset) of energy dissipation at various distances to failure in a typical experiment. The common color bar depicting the scale for the dissipation energy density ρ (J/m^2) is presented under the first panel. The spatial extent of the cascades extracted using the autocorrelation of the thresholded maps is denoted by the red bracket in the inset. (b) Evolution of clusters within a cascade [second panel in (a), at $\delta \simeq 0.025$] with colors representing unique cluster IDs. The center of mass of each cluster is shown in the background with a marker of the same color as the cluster. Here, the third axis is time. The largest clusters appear in multiple slices of time. Scaling of the size (in terms of dissipated energy) (c) and duration (d) of cascades, normalized by their maximum values, as a function of their characteristic spatial extent ξ, normalized by the system size L. Inset in (c): pair correlation function of the centers of mass of the clusters within a cascade permitting to extract the fractal dimension $d_f \simeq 1.15$. (e) Distribution of the cascade sizes obtained during the whole duration of experiments (diamonds) and in the vicinity of final failure (circles). (f) Distribution of waiting time between cascades. The waiting time is defined as the difference in time stamps of the arrival of two successive avalanches $\tau_w(\mathrm{s}) = t_i(\Delta_{\mathrm{ini}}) - t_{i-1}(\Delta_{\mathrm{ini}})$. Inset: distribution of waiting times considered as the difference in value of force $\tau_F(\mathrm{N}) = F_i - F_{i-1}$. (g) Fractal analysis of the spatial distribution of the seeds of the precursors in a typical experiment (inset) showing a behavior reminiscent of a spatial Poisson process ($d_f \simeq 2$). The statistical analyses are based on data recorded during ten experiments.

$\beta \simeq 1.30$, respectively. This difference results from the increase of the size of the largest precursors upon approaching failure (see Supplemental Material Sec. S4A [46,60]). The exponent β is connected later with the marginal stability of the material elements [61,62] that is investigated in Sec. IV A.

Finally, we characterize the correlations in the sequence of damage cascades. The distribution $P(\tau_{\mathrm{w}})$ of waiting times separating two successive damage cascades is shown in Fig. 2(f). It follows an exponential law $P(\tau_{\mathrm{w}}) \propto e^{-\tau_{\mathrm{w}}/\tau^{\star}_{\mathrm{w}}}$, defining a characteristic waiting time $\tau^{\star}_{\mathrm{w}}$. This result is at odds with the power-law distribution of waiting times separating acoustic events in compression experiments [21–23]. To confirm our observation, we perform additional experiments with a loading rate v_{ext} twice smaller. Interestingly, we also measure an exponential distribution but with a characteristic waiting time about twice larger [see Fig. 2(f)]. We thus replace the waiting time τ_{w} by the force increment τ_{F} separating two successive precursors, so that distributions corresponding to different loading rates collapse on a single curve, as shown on the inset of Fig. 2(f). The exponential distribution of the waiting time, characteristic of uncorrelated events described by a Poisson process, suggests that precursors are triggered independently from each other. This is further confirmed by the spatial distribution of the seeds (first damage event) of precursors that we define as the center of mass of the cluster appearing at $t(\Delta_{\mathrm{ini}})$. The fractal analysis of the precursor seeds provides $C(r) \propto r^2$, a behavior reminiscent of spatially uncorrelated events [see Fig. 2(g)].

III. THEORETICAL MODELING OF COMPRESSIVE FAILURE

The statistical features of the precursors measured in our experiments strikingly remind us of the avalanche dynamics of elastic interfaces driven in disordered media. In these models, an elastic interface responds to a continuously increasing drive and exhibits scale-free avalanches or crackling noise [42–44]. The size, spatial extent, and duration of the avalanches are related by scaling laws with universal exponents that depend on the interface elasticity and its dimension. For interfaces with long-range elasticity, avalanches are formed by a set of correlated clusters that are spatially disconnected similar to damage clusters within a cascade observed in our experiments [see Fig. 2(b)]. Taking inspiration from Weiss *et al.* [40] and using the nonlocal theory proposed by Dansereau *et al.* [58], we derive below

an evolution equation of the damage field in the specimen for a compression test under force-control conditions. This theoretical formulation sheds light on the connection with models of driven disordered elastic interfaces. We provide here the main ingredients of the derivation of the damage evolution law, the detailed calculations being presented in the Supplemental Material Secs. S3A–S3D [46].

First, we assume that the material behaves as an elastodamageable solid. We thus introduce a damage field $d(\vec{x},t)$ that describes the level of damage accumulated in the specimen at the location $\vec{x}$ and time t. Damage growth is inferred from a balance of energy by comparing two quantities: the local driving force $Y[d(\vec{x},t),t]$, which provides the rate of elastic energy released for an incremental growth of damage, and the damage resistance $Y_c[d(\vec{x},t)]$, which provides the material resistance to damage and corresponds to the rate of energy dissipated for an incremental growth of damage. The first quantity is similar to the elastic energy release rate introduced in fracture mechanics, which drives crack propagation and is a quadratic function $Y \propto \sigma_\circ^2$ of the nominal compressive stress $\sigma_\circ = F/(LW)$ applied by the test machine [63,64]. The damage resistance is equivalent to the fracture energy introduced in fracture mechanics. Note that in our model, Y_c depends not only on $\vec{x}$ as precursors emerge from the material inhomogeneities, but also on d as a damage event in $\vec{x}$ may change the subsequent failure resistance in the same material element. The damage then increases in the material element $\vec{x}$ if the local value of the driving force $Y(\vec{x})$ reaches the material resistance $Y_c(\vec{x})$.

To describe the damage field fluctuations resulting from the material heterogeneities, we introduce a reference damage level $d_\circ = \langle d(\vec{x},t_\circ)\rangle$ and the damage field perturbations $\Delta d(\vec{x},t) = d(\vec{x},t) - d_\circ$ over the time $\delta t = t - t_\circ \ll t_\circ$ to ensure that $\langle \Delta d(\vec{x},t)\rangle_{\vec{x}} \ll d_\circ$. The driving force and the damage resistance can then be linearized as $Y[d(\vec{x},t),\sigma_\circ] = Y_\circ(d_\circ,\sigma_\circ) + \Delta Y[\Delta d(\vec{x},t),\sigma_\circ]$ and $Y_c[d(\vec{x},t)] = Y_{c\circ}(d_\circ) + \Delta Y_c[\Delta d(\vec{x},t)]$. The zero-order equation $Y_\circ(d_\circ,\sigma_\circ) = Y_{c\circ}(d_\circ)$ provides the relationship between the reference damage level $d_\circ$ and the reference applied load $\sigma_\circ = \sigma(t_\circ)$. In the following, we investigate how the damage field perturbations $\Delta\dot{d}(\vec{x},t) \propto \Delta Y[\Delta d(\vec{x},t),\sigma_\circ] - \Delta Y_c[\Delta d(\vec{x},t)]$ evolve over time. We write the total driving force as the sum of three terms [40,58]

$$\Delta\dot{d}(\vec{x},t) \propto \mathcal{K}(\sigma_\circ)[v_m(\sigma_\circ)t - \Delta d(\vec{x},t)] + \psi(\sigma_\circ) * [\Delta d(\vec{x},t) - \langle \Delta d\rangle_{\vec{x}}] - y_c[\vec{x}, d(\vec{x},t)]. \quad (1)$$

The first (local) term comprises the effect of the driving by the test machine, where the driving speed $v_m \propto v_{ext}$ sets the damage growth rate. Considering a pseudo-interface of position $\Delta d(\vec{x},t)$, this term acts as a rigid plate moving at a speed v_m and pulling on the interface with springs of stiffness $\mathcal{K}$ (see Supplemental Material Fig. S3 [46] for a schematic representation). The second term is nonlocal. It describes the interactions within the specimen, and its value in $\vec{x}$ depends on the damage level $\Delta d(\vec{x},t)$ everywhere in the specimen. In practice, the kernel $\psi(\sigma_\circ)$ [provided in Eq. (B1)] describes the spatial structure of the redistribution of driving force taking place in the aftermath of an individual damage event. It decays as $\psi \propto 1/r^2$ [40,58]. Its angular dependence is shown in Fig. 3(a) for the particular case of uniaxial compression. It exhibits a quadrupolar symmetry with nonpositive regions (in blue). Hence, only a fraction of the neighboring elements are reloaded in the aftermath of a damage event, while the others (located above and below the damaged element) are actually unloaded. The third term represents the effect of material disorder. Its spatial average is close to zero as the contribution of the hardening $\langle \Delta Y_c\rangle_{\vec{x}} = \eta\langle \Delta d\rangle_{\vec{x}}$ (where η is a hardening parameter and observed in our experiments) is taken into account in the first term [see Supplemental Material Sec. S2 and Figs. S2(b) and S2(c) [46]]. The presence of $d(\vec{x},t)$ as an argument of the disorder term implies that the evolution equation (1) is strongly nonlinear, leading to the rich phenomenology that we now discuss.

Equation (1) provides a clear connection between damage evolution and disordered elastic interfaces: The accumulated damage field is analogous to a 2D elastic interface $\Delta d(\vec{x},t)$ driven at the speed v_m through a 3D disordered medium (see Supplemental Material Sec. S3E, Fig. S3 [46]). As a result, damage is expected to grow through bursts characterized by scaling laws involving critical exponents reminiscent of the

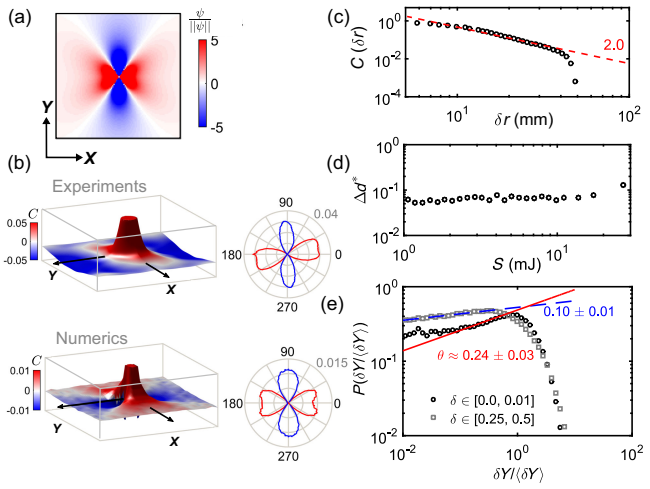

FIG. 3. (a) Angular distribution of the long-range interaction kernel derived theoretically for the case of uniaxial compression. (b) 2D autocorrelation map of the incremental damage field of precursors and angular distribution of the correlations at a fixed distance as obtained from the 50 largest avalanches measured in one of our experiments and our numerical simulations. (c) Variations of the correlation function of the incremental damage field with distance along the horizontal x axis and comparison with the scaling $\psi \propto 1/\delta r^2$ of the theoretical interaction kernel (dashed line). (d) Variations of the depth Δd^* of the damage cascade with the cascade size S. (e) Distribution of the local distance to failure $\delta Y(\vec{x})$ close and far from failure.

so-called depinning transition. As a first test of our model, we compare the theoretically predicted exponents with the one measured experimentally. Investigating the avalanche dynamics of 2D interfaces with nonpositive interactions in the context of amorphous plasticity, Lin *et al.* [61,65] predicted the exponent values $\beta = 1.51$, $d_f = 1.10$, and $z = 0.57$ that agree reasonably well with the ones measured in our experiments. Corrections to these predictions from the numerical solution of the evolution equation (1) are provided at the end of our manuscript in Sec. VIII. They improve further the agreement with the experimentally measured exponents.

Despite the ability of this approach to describe the scaling behavior of precursors, we note that two important features of the damage evolution equation (1) differ from standard models of driven elastic interfaces. First, the long-range elastic interactions result in both reloading and unloading of material elements in the aftermath of a damage event. Second, a subtler but more important feature is that the evolution equation (1) describes a nonstationary depinning scenario culminating in a bifurcation at the localization threshold. In the following, we examine these aspects in detail and discuss their implications for the damage accumulation process preceding failure.

IV. ATYPICAL ASPECTS OF DAMAGE EVOLUTION AS A DRIVEN DISORDERED ELASTIC INTERFACE

A. Nonpositive elastic interactions

We describe below a methodology that we employ to characterize the elastic interactions driving the cooperative dynamics of damage. This method takes advantage of our full-field characterization of damage precursors. Indeed, it turns out that the spatial distribution of events within an avalanche encrypts the range and the anisotropy of the elastic interactions, as we see below. The first step consists of computing the incremental damage field $\delta d(\vec{r})$ during an avalanche. Its 2D autocorrelation function $C(\vec{\delta r}) = \langle \delta d(\vec{r}) \cdot \delta d(\vec{r} + \vec{\delta r}) \rangle_{\vec{r}}$ averaged over several avalanches is presented in Fig. 3(b). The angular distribution (at a fixed distance) shows a clear quadrupolar symmetry similar to the redistribution pattern of the theoretical interaction kernel [Fig. 3(a)]. Remarkably, the correlation along the horizontal axis where the reloading is maximal, decays as $C(\delta r) \propto 1/\delta r^2$ [see Fig. 3(c)], a behavior also in line with the theoretical predictions of the elastic kernel, Eq. (B1). These observations support further the applicability of the nonlocal damage mechanics to our experiments.

The presence of an unloading region in the interaction kernel has several important implications. First, at the scale of a material element, the approach to failure is nonmonotonic as the local driving force for damage can both increase and decrease over time. As a result, the probability that an element damages more than once during a cascade is low. In practice, the depth of the avalanches Δd^* defined as the average damage increment of the elements involved in the cascade is constant and does not vary with the precursor size S, as shown in Fig. 3(d) (see also Supplemental Material Sec. S4A [46]). This is at odds with the behavior of driven elastic interfaces with positive interactions for which the depth of avalanches scales with their size.

Another crucial, yet more subtle difference relates to the distribution of the net driving force $\delta Y(\vec{x}) = Y_c(\vec{x}) - Y(\vec{x})$ that controls the (marginal) stability of the specimen. $\delta Y(\vec{x}) > 0$ provides the increment of driving force required for triggering damage. Its distribution computed over all the material elements is expected to scale as $P(\delta Y) \propto \delta Y^\theta$ [61,62,65–67]. Positive interactions lead to $\theta = 0$, pointing out the presence of a finite number of material elements close to failure. On the contrary, the number of elements close to failure vanishes for sign-changing interactions, leading to $\theta > 0$. The experimental determination of the exponent θ is quite challenging, as it requires *a priori* the knowledge of the material disorder. In practice, we circumvent this difficulty by computing the driving force $Y(\vec{x}, t)$ [according to Supplemental Material Eq. (S4) [46]] at each time step for each material element and determine $Y_c[d(\vec{x}, t)]$ retrospectively from the value of $Y(\vec{x}, t)$ when the material element damages [see Appendix A 4, and Supplemental Material Sec. II and Fig. S2(a) [46] for details on the method]. Figure 3(e) shows the distribution $P(\delta Y / \langle \delta Y \rangle)$ close to and far from localization. In both cases, we measure a positive exponent $\theta > 0$, a particularly nontrivial property that comes in support of the proposed model. Interestingly, θ increases as the specimen approaches failure, a feature that possibly arises from the nonstationary nature of the evolution equation (1). The exponent θ has been shown to be related to $\beta = 2 - (\theta/\theta + 1)(d/d_f)$ [61] that characterizes the distribution of precursor size S. This scaling relation predicts a slight decrease of β upon approaching failure, a subtle effect that is consistent with our experimental observations. A similar trend of an increasing θ has been reported in direct simulations of sheared amorphous solids that are also characterized by sign-changing interactions [62,68].

B. Divergence of precursors

We now come back to the observations made in Figs. 1(d) and 2(a) of an increase of the size and the spatial extent of precursors close to failure. As shown in Fig. 4(a), the average precursor size increases as a power law with the distance to failure $\langle S \rangle \sim 1/\delta^{-\alpha}$ where $\alpha \simeq 0.57$. Following the scaling relations $S \propto \xi^{d_f}$ and $T \propto \xi^z$, the associated length and timescales then also diverge upon approaching failure. This is confirmed by the variations of the precursor spatial extent directly

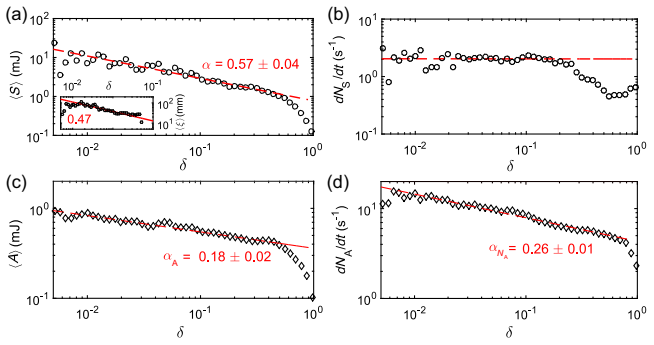

FIG. 4. Variation with distance to failure of (a) the average precursor size $\langle S \rangle$, the average spatial extent of precursors $\langle \xi \rangle$ in the inset, (b) the activity rate dN_S/dt, (c) the average size of load drop events $\langle A \rangle$, and (d) the event activity rate dN_A/dt. While S and dN_S/dt characterize the intermittent damage activity under force-controlled conditions, A and dN_A/dt are relevant for displacement-imposed conditions. The product of both quantities $dE_d/dt = \langle S \rangle dN_S/dt = \langle A \rangle dN_A/dt$ provides the dissipation rate that also diverges as $dE_d/dt \sim \delta^{-\alpha}$ with $\alpha = 1/2$.

measured from our local analysis (see Supplemental Material Sec. 1 D [46]) in the inset of Fig. 4(a).

Notably, the activity rate dN_S/dt, i.e., the number of cascades per interval of time, is rather constant during damage accumulation; see Fig. 4(b). This is in line with our previous observation of an exponential distribution of waiting times, supporting further that precursors emerge from a (random) Poisson process. As the dissipation rate dE_d/dt during the intermittent damage evolution writes as the product of the average precursor size with the precursor rate $dE_d/dt = \langle S \rangle dN_S/dt$, we obtain $dE_d/dt \propto 1/\delta^{-\alpha}$. As argued in the next section, the divergence of the dissipation rate upon approaching peak load is reminiscent of damage localization, a feature that results from the loss of stability of the specimen. To further test this idea, we reanalyze our data considering the actual displacement-imposed conditions that also give rise to damage localization at peak load. The dissipation rate then writes as the product of the average load drop size $\langle A \rangle$ with their activity rate dN_A/dt [refer to Supplemental Material Sec. 1 B and Fig. S1(b) [46] for the definition of precursors under displacement-imposed loading conditions]. We observe that both load drops $\langle A \rangle \propto \delta^{-\alpha_A}$ and precursor rate $dN_A/dt \propto \delta^{-\alpha_{N_A}}$ diverge on approaching localization; see Figs. 4(c) and 4(d). The exponent $\alpha = \alpha_A + \alpha_{N_A} \simeq 0.44$ characterizing the divergence of the dissipation rate under displacement-imposed conditions is close to $1/2$, as expected, and accounts for the numerical observations of Girard *et al.* [33] who reported $dE_d/dt \propto \delta^{-0.4}$.

V. DAMAGE LOCALIZATION: DEPINNING TRANSITION OR STANDARD BIFURCATION?

The divergence of the precursor size, and hence of the characteristic timescale and length scale of precursors upon approaching failure, supports *a priori* the interpretation of compressive failure as a critical point [26,40]. However, the comparison between the scaling exponents predicted by the critical point scenario and the exponents measured in our experiments tells a different story (see Table I).

To explain the difference between the theoretical predictions and our experimental observations, we further develop the model proposed in Sec. III. We focus on the nonstationary aspects of the evolution equation (1), namely, the stiffness $\mathcal{K}$ and the driving speed v_m that are given by the following expressions:

$$\mathcal{K}(\sigma_\circ) = \left.\frac{\partial(Y_{c\circ} - Y_\circ)}{\partial d_\circ}\right|_{\sigma_\circ},$$
$$v_m(\sigma_\circ) = v_{ext}\left(\frac{\partial Y_\circ/\partial \sigma_\circ|_{d_\circ}}{\mathcal{K}(\sigma_\circ)}\right). \quad (2)$$

$\mathcal{K}$ controls the stability of the damage evolution. Indeed, a negative value of $\mathcal{K}$ implies that the net driving force $Y - Y_c$ increases with the damage level, leading to its unstable growth and thus failure. It turns out that $\mathcal{K}$ goes to zero upon approaching peak load (see Supplemental Material Sec. S3F [46]), in line with the stability condition under force-controlled conditions. The driving speed v_m is inversely proportional to $\mathcal{K}$ and hence goes to infinity. A linear expansion of the damage evolution equation close to peak load $\sigma_\circ < \sigma_c$ (see Supplemental Material Sec. S3G [46]) provides the asymptotic behavior of the damage growth rate $\dot{\Delta d} \sim 1/\sqrt{\delta}$. As $\dot{\Delta d} \propto v_m$, owing to Eq. (2) we obtain $v_m \sim 1/\sqrt{\delta}$ and thus, $\mathcal{K} \sim \sqrt{\delta}$.

What then are the consequences of the divergence of the speed of the pseudo-interface at peak load? As the rate of dissipated energy is controlled by the damage growth rate, one expects $dE_d/dt \propto 1/\sqrt{\delta}$. Considering the intermittency of damage evolution, the dissipation rate writes as the product of the precursors' size with the precursors' rate, $dE_d/dt = \langle S \rangle dN_S/dt$. As dN_S/dt remains constant during the experiment [Fig. 4(b)], a feature expected for disordered

TABLE I. Comparison between the exponents predicted by the critical point scenario that interprets failure as a depinning transition and the exponents measured in our experiments. The three exponents provided below describe the divergence as $\delta^{-\gamma}$ of the avalanche size S, its spatial extent ξ, and its duration T upon approaching failure. The theoretical exponents describe the behavior of a driven 2D interface with long-range nonpositive elastic interactions approaching the depinning transition [26,61].

	Critical point scenario		Experiments	
	γ	Prediction—2D	γ	
S	νd_f	1.27	α	0.57
ξ	ν	1.16	α/d_f	0.53
T	νz	0.66	$z\alpha/d_f$	0.28

elastic interfaces, it follows that $\langle S\rangle \sim 1/\sqrt{\delta}$, a prediction that accounts for our experimental observations.

The implication of our model is clear: The divergence of the size of the precursors close to failure, and hence the divergence of the length scale and timescale of the fluctuations, results from the presence of a standard bifurcation at peak load. The progressive loss of stability of the specimen upon approaching peak load is accompanied by a divergence of the damage growth rate (and thus, a divergence of the precursor size), a behavior that has nothing to do with the presence of disorder. This mechanism is in stark contrast with the divergence of fluctuations near a critical point, a feature that vanishes if the disorder is shut down.

To further support this claim, we rewrite the damage evolution law (1) using the new variable $\underset{\sim}{d}(\vec{x}) = d(\vec{x})\sqrt{\delta}$. The obtained expression ensures a straightforward connection with standard (stationary) depinning models [42,44]:

$$\Delta\dot{\underset{\sim}{d}} \propto \mathcal{K}_0[v_{\mathrm{m}0}t - \Delta\underset{\sim}{d}(\vec{x},t)] + \psi(d_\circ\sqrt{\delta})/\sqrt{\delta} * [\Delta\underset{\sim}{d}(\vec{x},t) - \langle\Delta\underset{\sim}{d}\rangle_{\vec{x}}] - y_{\mathrm{c}}[\vec{x},\underset{\sim}{d}(\vec{x},t)]. \quad (3)$$

Under this form, the evolution equation displays both a constant stiffness $\mathcal{K}_0 = \mathcal{K}/\sqrt{\delta}$ and a constant driving speed $v_{\mathrm{m}0} = v_{\mathrm{m}}\sqrt{\delta}$. The normalized damage field $\underset{\sim}{d}$ behaves as an elastic interface driven at constant finite speed during the whole damage accumulation regime. As a result, the specimen remains at a fixed distance to the depinning transition that corresponds to the limit $v_{\mathrm{m}0} \to 0$ and $\mathcal{K}_0 \to 0$. Our conclusions are in stark contrast with a depinning scenario where the divergence of the precursory activity results from the interpretation of compressive failure as a critical transition and the evolution of the specimen toward this critical point. In other words, the increasing applied load drives the specimen toward instability without driving it toward more criticality. The intricate connection between damage precursors and localization is illustrated in Fig. 5.

We now highlight the strategic value of our findings to structural health monitoring. In our theoretical description of compressive failure, the evolution of precursors is described by robust scaling laws that are independent of the material properties and the loading conditions. In particular, as they apply for both force- and displacement-driven experiments, they serve as early warning signals of impending failure.

VI. FAILURE PREDICTION FROM PRECURSORY ACTIVITY

We now harness the scaling behavior of the precursors and bring an experimental proof of concept of their predictive power by inferring the residual lifetime of our specimen. We perform a retrospective failure prediction using the cascade size S measured during the damage accumulation regime. To do so, we follow the idea of Anifrani *et al.* [69] and use the methodology proposed by Mayya *et al.* [70]. Considering a time series of measured precursory activity for the equivalent-force-controlled experiment, the normalized distance to failure here writes as $\delta = (t_{\mathrm{c}} - t)/t_{\mathrm{c}}$ where $t = 0$ corresponds to $F = F_{\mathrm{el}}$ and $t = t_{\mathrm{c}}$ corresponds to $F = F_{\mathrm{c}}$. We rewrite the scaling law for the cascade size variations as

$$\langle S\rangle = S_0/\sqrt{t_{\mathrm{c}} - t}, \quad (4)$$

where S_0 is a constant. Rearranging the terms, we obtain $\langle S\rangle^2 t = \langle S\rangle^2 t_{\mathrm{c}} + S_0$, an expression that can be used for performing a linear regression of our experimental dataset (t, S) shown in Fig. 6(a). The average size of the precursors is obtained over a nonoverlapping time window of 10 s. The prediction is made at time t_{cur} so that only the precursors recorded at time $t < t_{\mathrm{cur}}$ can be used for the prediction. Note, however, that we use only a short period (here 100 s) before t_{cur} to make the prediction.

The linear regression provides $t_{\mathrm{c}}^{\mathrm{pred}}$ that is shown in Fig. 6(b) as a function of t_{cur}. As shown in the inset, the error on the predicted failure time reduces as the prediction is made closer to the actual failure time t_{c}. The prediction

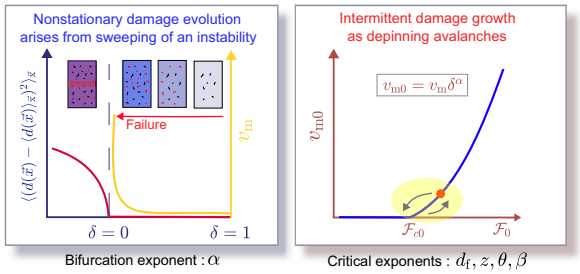

FIG. 5. Interpretation of the two phenomena underlying compressive failure of disordered solids. The left panel describes the behavior of the specimen as it is driven to failure. The amplitude of the fluctuations of the damage field (in red) and the dissipation rate (yellow) increase near failure ($\delta = 0$). The spatial variations $\langle(d(\vec{x}) - \langle d(\vec{x})\rangle_{\vec{x}})^2\rangle_{\vec{x}}$ of the accumulated damage are essentially zero before peak load ($\delta < 0$) but rapidly increase after localization ($\delta > 0$). The state of the specimen bifurcates from a homogeneously growing damage to a localized damage growth. This bifurcation is preceded by an increase $v_{\mathrm{m}} \sim \delta^{-\alpha}$ of the dissipation rate, and thus an increase of $\langle S\rangle \sim \delta^{-\alpha}$ of the fluctuation amplitude. The right panel describes the process of damage growth at a fixed distance to failure. By renormalizing the nonstationary features of the evolution equation [see Eq. (3)], we realize that the damage field behaves as an elastic interface driven in a disordered medium at constant speed. $v_{\mathrm{m}0} \simeq v_{\mathrm{m}}\delta^{\alpha}$ at a fixed distance above the critical point (here, the depinning transition) even when we reach peak load ($\delta = 0$) and thus bifurcation.

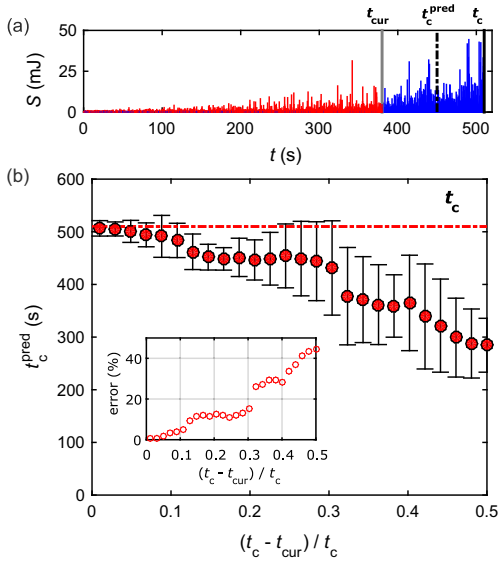

FIG. 6. (a) Time-series data of failure precursors obtained during the compression test and data available for prediction (red) at t_{cur}. (b) Variation of the predicted remaining lifetime at different instances t_{cur} represented as a fraction of the time to failure. The error bars provide intervals with 90% confidence levels. Inset: error on the predicted remaining lifetime.

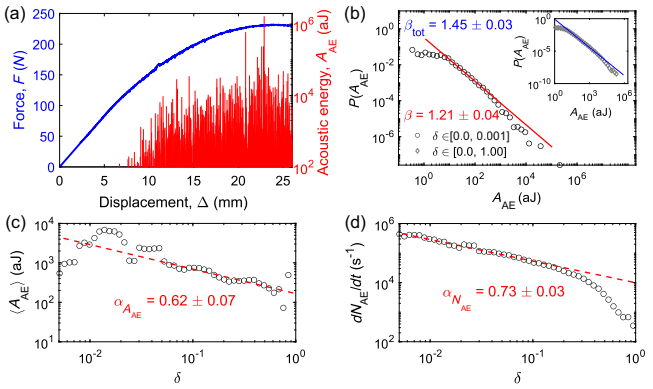

FIG. 7. (a) Acoustic emissions recorded during a typical experiment of compressive failure. (b) Distribution of acoustic event energy recorded during the whole duration of experiments (inset) and close to failure (main panel). Variations of the average value of (c) the acoustic energy A_{AE} and (d) their activity rate dN_{AE}/dt with distance to failure δ.

lies within 10% error when the prediction is made in the last 25% of the total lifetime. Note that the same methodology can be implemented using the duration or the rate of events (under displacement-controlled conditions only), thus providing several independent measurements to forecast final failure. Interestingly, the predictions are conservative by providing shorter residual lifetime than the actual one. Importantly, the proposed methodology does not require monitoring from the beginning of the damage accumulation phase. The robustness of our method strongly argues that the statistical analysis of failure precursors based on the proposed scenario is an efficient quantitative tool of damage monitoring and lifetime prediction of structures.

VII. ACOUSTIC EMISSIONS

We now verify the generality of our results and their applications to standard brittle solids. To this effect, we analyze the acoustic emissions accompanying damage growth in our experiments (see Appendix A 1 for experimental details). A typical acoustic emission time-series record is shown in Fig. 7(a). First, we observe bursts of acoustic emissions separated by silent periods, a behavior typical of compressive failure of brittle disordered materials. Then, we see that the acoustic activity intensifies closer to peak load, near localization, a behavior that is also observed close to failure in standard brittle solids, and that we explore in more detail below. The distribution of acoustic event energy is shown in Fig. 7(b) and in the inset. It follows a power law with an exponent $\beta_{\mathrm{tot}_{AE}} \simeq 1.45$ that is slightly smaller when we consider only the acoustic emissions close to failure $\beta_{AE} \simeq 1.21$. Tracking now the evolution of the acoustic activity, we find that the energy $\langle A_{AE} \rangle$ of the acoustic events increases as $\langle A_{AE} \rangle \propto \delta^{-\alpha_{A_{AE}}}$ upon approaching failure; see Fig. 7(c). The acoustic activity rate $dN_{AE}/dt \propto \delta^{-\alpha_{N_{AE}}}$ also increases as a power law upon approaching failure; see Fig. 7(d). As a result, the rate of acoustic energy dE_{AE}/dt defined as the product of the average acoustic event energy with the activity rate $dE_{AE}/dt \propto \langle A_{AE} \rangle dN_{AE}/dt$ increases as $dE_{AE} \propto \delta^{-\alpha_{AE}}$ where $\alpha_{AE} = \alpha_{A_{AE}} + \alpha_{N_{AE}} \simeq 1.35$. A comparison of the exponents measured in our experiments with the one reported in the literature shows that damage spreading in our experimental system shares strong similarities with damage spreading in standard brittle solids. In particular, the exponents $\beta_{\mathrm{tot}_{AE}} \simeq 1.4$ and $\alpha_{N_{AE}} \simeq 0.7$ measured in our experiments are similar to the one measured in rocks [23,71,72], coal [73], and concrete [26]. Beyond confirming the applicability of our experimental and theoretical findings to a broad range of brittle materials, these results confirm the versatility of acoustic emissions analysis as a damage monitoring tool.

We would like to discuss the intricate connection between acoustic emissions [74] and the mechanical energy cascades that are thoroughly characterized in our experiments (see Secs. II B and II C). We clearly observe that acoustic events do not correspond to the damage cascades characterizing the mechanical response of the specimen. First, we find that their number (typically 10^3) during an experiment is much larger than the number of mechanical precursors (typically 10^2). Then, we observe that the exponent α_{AE} characterizing the increase of emitted acoustic energy upon approaching failure is much larger than the exponent α describing the increase of the dissipated rate of mechanical energy. Finally, we observe that the rate of acoustic events increases upon approaching

failure, an observation in stark contrast with the constant activity rate observed for damage cascades; see Fig. 4(b).

We infer that the acoustic emissions may rather be reminiscent of the dissipative processes taking place at much lower spatiotemporal scales within damage cascades. Such a scenario also agrees with the power-law distribution of interevent waiting time of acoustic events [23,52] that contrasts with the exponential distribution observed here for damage cascades; see Fig. 2(f). A deeper analysis of our experimental data may be needed to understand the connection between mechanical precursors and acoustic events. Nevertheless, their increase upon approaching failure may be harnessed for tracking damage growth and predicting the residual lifetime of structures after calibration of material specific exponents [70].

VIII. NUMERICAL SOLUTION OF THE DAMAGE EVOLUTION EQUATION

To conclusively validate our interpretation of the nonstationary avalanche dynamics preceding compressive failure, we numerically solve the damage evolution equation (1) using a 2D cellular automata (see Appendix B) for both force- (Supplemental Material Sec. S4A [46]) and displacement- (Supplemental Material Sec. S4B [46]) control conditions. We recover that intermittent damage accumulation culminates in a bifurcation that manifests as the emergence of a localization band at peak load [Supplemental Material Figs. S4(a), S4(b), S5(a), and S5(b) [46]]. The exponents characterizing the damage cascades are measured numerically [Supplemental Material Figs. S4(c)–S4(j) and S5 (c)–S5(j) [46]] using the methods employed for analyzing the experimental data, thus allowing for a systematic comparison with the statistical features of the precursors measured experimentally. Numerical and experimental exponents are provided in Table II. We also proceed to a comparison with exponent values reported in the literature (see Supplemental Material Table S2 [46]). The good agreement supports our theoretical framework as an adequate description. Importantly, the similarities between the statistics in force and equivalent-force control validate our method of reconstruction of the precursors from our experimental dataset and interpretation of failure built from the analyses. We also verify numerically the method employed to characterize the elastic interactions from the incremental damage field in Fig. 3(b).

TABLE II. Exponents from experiments and the numerical model.

	Definition	Experiments	Simulations[a]
d_f	$S \propto \xi^{d_f}$	1.07 ± 0.07	1.15
z	$T \propto \xi^{z}$	0.53 ± 0.11	0.62
θ	$P(\delta Y) \propto \delta Y^{\theta}$	0.24 ± 0.03	0.35 (0.18)
β	$P(S) \propto S^{-\beta}$	1.30 ± 0.11	1.36 (1.34)
α	$S \propto \delta^{-\alpha}$	0.57 ± 0.04	0.48 (0.60)
z/d_f	$T \propto S^{z/d_f}$	0.49 ± 0.14	0.53 (0.64)
β_{tot}	$\beta_{tot} = \beta + \frac{2-\beta}{\alpha}$	2.32 ± 0.18	2.2 (2.13)

[a]Values in brackets are from the equivalent-force-control scenario.

IX. IMPLICATIONS AND CONCLUSION

We would like to conclude by highlighting the implications of our findings. First, our results may be relevant for any brittle solids such as rocks, concrete, and mortar, the generality of our approach being bonded to damage mechanics that we use to describe our experiments (see Appendix 2). By showing that compressive failure is not a critical phase transition, but instead a standard bifurcation, we pave the way for reliable predictions of the failure load of brittle solids and the use of precursory events to anticipate their forthcoming failure. Indeed, this finding implies that the stability analysis of a homogeneous specimen is sufficient to predict the failure load of disordered solids. This approach used in our study captures the emergence of the localization band at peak load and, more generally, the stress-strain response of the specimen. Further experimental validations of the application of these concepts to more complex materials are a part of ongoing studies. Another direct implication of our finding is the prediction of the forthcoming failure from the statistics of precursors. The interpretation of compressive failure as a standard bifurcation provides robust scaling laws that can be harnessed to predict failure.

We also highlight the implications of our work for a larger class of phenomena. Compressive failure is an archetypical example of seemingly critical phenomena, as it is preceded by precursors with diverging size and duration upon approaching failure. We show that this apparent criticality is not bounded to the presence of a critical point. Instead, we show that a standard bifurcation in the presence of disorder and long-range interactions results in an intermittent response with fluctuations that diverge on approaching the bifurcation point. We expect these ideas to be relevant for understanding the relationship between intermittent plastic flow and shear banding in amorphous solids, where the nature of the yielding transition and the localization has been vigorously debated during these recent years [61,68,75]. Our interpretation of the specimen being at a finite distance above the critical point as it evolves toward failure aligns well with the conclusion drawn by Lin *et al.* [62] in the context of amorphous plasticity. Using a discrete model of amorphous plasticity, they show that avalanche size diverges upon approaching failure. Yet, this divergence is not reminiscent of a critical behavior. Instead, they show that the avalanche size is controlled by the slope $d\sigma/d\epsilon$ of the stress-strain response. The scaling law $\langle S \rangle \propto [1/(d\sigma/d\epsilon)]$ proposed in their study is compatible with the one obtained in our experiments $\langle S \rangle \propto (1/\sqrt{\delta})$ [see Fig. 4(a)]. This further

supports the relevance of the scenario proposed here for sheared amorphous media.

In summary, we investigate experimentally the precursors to localization during compressive failure of 2D cohesionless soft cellular solids. This model system is shown to behave like a wide range of standard (and somehow more complex) brittle materials under compression. We use this simplified brittle disordered material to characterize in depth (i) the highly correlated sequence of spatially coherent clusters of failure events that compose precursors, (ii) the divergence of the size, the spatial extent, and the duration of these precursors upon approaching failure, (iii) the presence of the long-range elastic interactions decaying as $1/r^2$ that drives this cooperative dynamics, (iv) the power-law distributed acoustic bursts accompanying these damage cascades, and finally (v), the emergence of a localization band at peak load. We characterize the nonstationary statistics of the damage cascades observed during the damage accumulation regime prior to localization. We then derive from continuum damage mechanics an evolution equation of the damage field that is shown to account quantitatively for all the scaling properties measured experimentally. The avalanche dynamics of damage growth is thus shown to be reminiscent of a nonstationary depinning scenario that reconciles the two competing approaches proposed to describe compressive failure, namely, standard bifurcation and critical transition.

Ultimately, failure precursors are shown to be merely the by-products of the progressive loss of stability of the specimen as it approaches localization. Contrary to the critical transition scenario, specimens driven toward failure stay at a fixed distance to criticality. Nevertheless, the evolution of the statistical features of precursors can be harnessed to anticipate and even predict the forthcoming failure.

ACKNOWLEDGMENTS

The authors gratefully acknowledge financial support from Sorbonne Université through the Emergence Grant for the research project, "From damage spreading to failure in quasi-brittle materials," from CNRS and Satt-Lutech through the tech transfer project, "Development of a technology of predictive maintenance for materials and structures," and from the National Center for Space Studies for the project, "From diagnostic to prognostic in structural health monitoring".

APPENDIX A: EXPERIMENTAL CHARACTERIZATION OF PRECURSORS

1. Experimental setup

Our specimen consists of a hexagonal packing of about 1500 soft cylinders made of polypropylene placed in a transparent Plexiglas box of dimensions $205 \times 170 \times 30$ mm^3, as shown in Fig. 1(a). The cylinders are 25 mm long with a 5-mm diameter. Displacement is applied to the upper layer through a Plexiglas beam using an AG-X Shimadzu test machine. The force experienced by the specimen is measured using a 10-kN load cell and sampled at a rate of 100 Hz. During the test, images are recorded every 0.1 seconds from the lateral side of the box using a Baumer HXC20 camera with a resolution of 2048×1088 pixels and binarized using the open-source FIJI software [76]. Precursory activity recorded during ten experiments with loading rate of 2 mm/ min and two experiments with loading rate of 1 mm/ min are analyzed to determine the statistical structure of precursors. The peak load measured in our experiments is $F_c = 228 \pm 4$ N. Acoustic emissions are recorded during four of the ten experiments using two low-frequency sensors (type R3α from Mistras Group, Physical Acoustics) that are placed on the compression platens. The signals crossing the fixed threshold 27 dB from the transducers are preamplified (40 dB) and transferred to a PC1-2 acquisition system. A detailed analysis in a study of acoustic emissions during dislocations shows that the scaling exponents are robust even for the range of the timing parameters that may result in superposition of events [77]. Still, we account for the cellular nature of the packing and set the event detection time post the first crossing of threshold as well as the lockout time for signals after the event as 500 μs. Calibration of the timing parameters is performed by recording signals from pencil lead breaks on metallic rods placed within the cylindrical cells.

2. Cohesionless soft cellular solids under compression as model brittle solids

We justify here why the packings of cohesionless soft cells employed in our experiments can be considered as model materials to investigate the intermittent response of brittle disordered solids under compression. First, we show that our packings of soft cells behave like standard elastodamageable media, a description that has been shown to accurately describe the compressive response of brittle solids [5]. Then, we explain how friction between cells that control the nonelastic response of our packings leads to a mechanical response that is similar to the ones of brittle solids under compression.

First, we validate the applicability of damage mechanics to describe the average mechanical response of our packings of soft cells. We remind that elastodamageable solids behave elastically until some critical load level is reached. Then, damage (the level of which is described by an internal variable noted $d_\circ$) increases. The impact of damage on the mechanical response of the material is described by the decrease of the material Young's modulus $E(d_\circ)$ and the variations of its Poisson ratio $\nu(d_\circ)$ where $d_\circ$ is the accumulated damage. In our experiments, $d_\circ$ is obtained from the deviation of the cell geometry to cell circularity, a definition that is justified below.

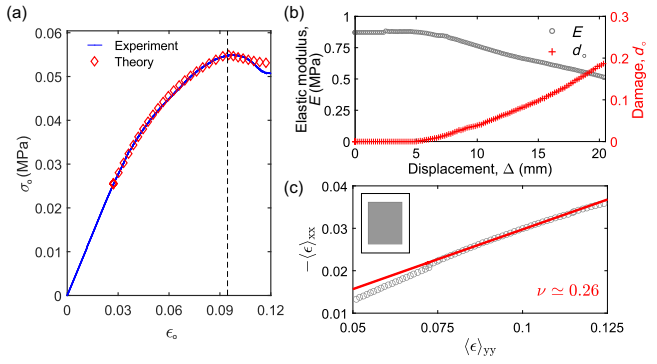

FIG. 8. Suitability of damage mechanics to describe the average mechanical response of the cohesionless frictional cellular solids used in our experiments. (a) Comparison of the mechanical response predicted by damage mechanics with the experimental stress-strain curve. (b) Variations of the elastic modulus and the average damage level during a representative experiment as inferred from the global mechanical response and our tracking of the cells' position. (c) Determination of the Poisson ratio ν inferred from the linear fit of the lateral strain vs the normal one after averaging over the central gray region of the specimen shown in the inset. $\nu \simeq \nu_\circ(d_\circ) = 0.26$ is found to be nearly constant and independent of $d_\circ$.

The Young's modulus of our packings is obtained from the instantaneous specimen stiffness $E = (1-\nu^2)\sigma_\circ/\epsilon_\circ$ leading to the following quadratic decrease: $E \simeq E_\circ - a_\circ d_\circ^2$. Its Poisson ratio $\nu \simeq 0.26$ obtained from the ratio $-\langle\epsilon_{xx}\rangle/\langle\epsilon_{yy}\rangle$ computed in the central region of the specimen [see Fig. 8(c)], is found to be constant throughout our experiments and nearly independent of the damage level $d_\circ$.

The force-displacement response predicted by elastodamageable theory is shown in Fig. 8(a). It results from the balance $Y[\sigma_\circ(d_\circ), E(d_\circ), \nu] = Y_c(d_\circ)$ between the elastic energy release rate Y and the damage energy Y_c (see Supplemental Material Sec. III. A [46] for the detailed calculation). The predicted behavior captures our experimental data very well. The macroscopic stress $\sigma_\circ$ and strain $\epsilon_\circ$ are computed here as parametric functions of the average damage level $d_\circ$,

$$\sigma_\circ(d_\circ) = \frac{E(d_\circ)}{\sqrt{1-\nu^2}}\sqrt{\frac{-2Y_{c\circ}(d_\circ)}{E'(d_\circ)}},$$
$$\epsilon_\circ(d_\circ) = \sqrt{1-\nu^2}\sqrt{\frac{-2Y_{c\circ}(d_\circ)}{E'(d_\circ)}}. \quad \text{(A1)}$$

The average damage resistance $Y_{c\circ}(d_\circ)$ is inferred from the displacement fields measured by tracking the cell positions, following the procedure described in Appendix A 4. Note that beyond capturing the average mechanical response of the packings of soft cells used in our experiments, elastodamageable theory captures the fluctuations around this average response, and in particular, the statistics of failure precursors in its most subtle details. The application of the elastodamageable theory to disordered brittle solids is described in Sec. III of the Supplemental Material [46], and the comparison of the predictions derived from this model with our experimental observations is summarized in Table II. Note also that the long-range interactions decaying as $1/r^2$, a unique feature of elastodamageable solids, is retrieved in our experiments [see Figs. 3(a)–3(c)]. Last but not least, elastodamageable theory predicts (see Supplemental Material Sec. 3F [46]) the emergence of localization at peak load, a prediction in perfect agreement with our experimental observations (see Appendix A. 5 for the experimental determination of the onset of damage localization).

The applicability of damage mechanics to our packings of soft cells supports the generality of our findings and their applicability to a broad range of brittle disordered solids. We now provide a microscopic interpretation of this seemingly surprising behavior. The inelastic behavior of our packings of soft cells is governed by the friction between neighboring cells. This rearrangement of the cells explains the local softening of the material that is appropriately described by a local decrease of the Young's modulus $E(d_\circ)$ within the theoretical framework of damage mechanics. Meanwhile, cell rearrangements alter the geometry of the initially circular cell. As a result, the deviation to cell circularity is appropriate for these rearrangements and the associated material softening, justifying the definition of the damage level $d_\circ$ employed in our study. Friction is very often considered as the central damage mechanism in standard brittle solids under compression. This is clearly evidenced by the large success of the Mohr-Coulomb theory (a model that directly derives from the assumption that the different regions of the material can slide on each other) in describing the inelastic response of brittle materials under compression.

Interestingly, Karimi *et al.* [48] previously noticed in their numerical work that soft granular solids can be described by damage mechanics. They also observed in their simulations that such systems failed through the emergence of a localization band at peak load and even noticed that the size of the failure precursors diverge as a power law, two observations in agreement with our experimental observations.

Overall, these various observations support our central assumption: Packings of frictional soft particles behave as elastodamageable solids, a conclusion already drawn by Houdoux *et al.* [78,79] from compression experiments carried out on standard granular solids.

3. Precursor size in an equivalent-force-control scenario

We explain here why the energy dissipated by damage during a precursory damage event follows the expression $S_{\text{global}} = (\Delta_{\text{end}} - \Delta_{\text{ini}})F_0/2$. We compute first the elastic energy stored in the specimen right before (for $\Delta = \Delta_{\text{ini}}$)

and right after (for $\Delta = \Delta_{\mathrm{end}}$) the precursory damage event. They follow $E_{\mathrm{el,ini}} = \Delta_{\mathrm{ini}} F_0/2$ and $E_{\mathrm{el,end}} = \Delta_{\mathrm{end}} F_0/2$, respectively. This leads to the following expression: $\Delta E_{\mathrm{el}} = E_{\mathrm{el,end}} - E_{\mathrm{el,ini}} = (\Delta_{\mathrm{end}} - \Delta_{\mathrm{ini}})F_0/2$ for the variation of the total elastic energy stored in the specimen during one precursory event. Note that this quantity is positive, meaning that the stored elastic energy does increase during a precursory event. We now compute the work of the external force during such an event. As the force is constant during the considered force-controlled scenario, we obtain $\Delta W = (\Delta_{\mathrm{end}} - \Delta_{\mathrm{ini}})F_0$. This quantity is defined positive and corresponds to the energy injected by the loading machine within the specimen during a precursory event. The determination of the energy dissipated by damage during a precursor is now in order. Observing that the energy injected by the loading machine during one precursor compensates exactly the new elastic energy stored in the specimen and the one dissipated by damage, one obtains $\Delta W = \Delta E_{\mathrm{el}} + S_{\mathrm{global}} \Rightarrow S_{\mathrm{global}} = \Delta W - \Delta E_{\mathrm{el}} = (\Delta_{\mathrm{end}} - \Delta_{\mathrm{ini}})F_0/2$. Interestingly, this balance of energy during one precursor can be understood graphically from the force-displacement response of the specimen during the event. As shown in Fig. 1(c), the work $\Delta W = \int_{\Delta_{\mathrm{ini}}}^{\Delta_{\mathrm{end}}} F(\Delta) d\Delta = F_0 \int_{\Delta_{\mathrm{ini}}}^{\Delta_{\mathrm{end}}} d\Delta = (\Delta_{\mathrm{end}} - \Delta_{\mathrm{ini}})F_0$ of the external force during one precursor corresponds to the area of the rectangle located below the force plateau. This rectangle can be divided into two other rectangles of similar size $(\Delta_{\mathrm{end}} - \Delta_{\mathrm{ini}})F_0/2$, one of them corresponding to the additional stored energy ΔE_{el} [represented in gray in Fig. 1(c)], while the other one corresponding to the dissipated energy $\Delta E_{\mathrm{d}} = S_{\mathrm{global}}$ (represented in yellow). This equipartition of energy between the new stored elastic energy and the dissipated one provides a simple way to track the size of failure precursors during the phase of damage accumulation.

4. Tracking damage evolution

The continuous image acquisition allows for the tracking of both position and circularity (used here to define damage) of individual cells. We then compute the displacement fields $u_x(\vec{x}, t)$ and $u_y(\vec{x}, t)$ and the damage field $d(\vec{x}, t)$ of the effective elastodamageable medium following the coarse-graining procedure described in Glasser and Goldhirsch [80]. To resolve the damage cascades from the image stack, we refer to the macroscopic response where an equivalent-force-control scenario is constructed from the sequence of load drops. We thus obtain the start and end of each damage cascade that are noted $t(\Delta_{\mathrm{ini}})$ and $t(\Delta_{\mathrm{end}})$, respectively. The damage events belonging to the image stack constituting the cascades are then clustered based on their connectivity (26-connected neighborhood). This procedure provides a space-time dissipation map of failure precursors composed of a series of highly correlated clusters. We derive the strain field as $\epsilon_{\mathrm{xx}}(\vec{x}) = (du_x/dx)$, $\epsilon_{\mathrm{yy}}(\vec{x}) = (du_y/dy)$ and $\epsilon_{\mathrm{xy}}(\vec{x}) = \frac{1}{2}[(du_x/dy) + (du_x/dy)]$. The field of elastic energy stored in the specimen per unit volume is then obtained from the relation

$$E_{\mathrm{el}}^{\mathrm{local}}(\vec{x}, t) = \frac{E_{\mathrm{local}}(\vec{x}, t)}{2(1-\nu^2)}[\epsilon_{\mathrm{xx}}^2(\vec{x}, t) + \epsilon_{\mathrm{yy}}^2(\vec{x}, t) + 2\nu\epsilon_{\mathrm{xx}}(\vec{x}, t)\epsilon_{\mathrm{yy}}(\vec{x}, t) + 2(1-\nu)\epsilon_{\mathrm{xy}}^2(\vec{x}, t)]. \tag{A2}$$

The field of damage driving force is obtained as $Y[d(\vec{x}, t)] = (dE_{\mathrm{el}}^{\mathrm{local}}/dd)$. The field of damage resistance $Y_{\mathrm{c}}[d(\vec{x}, t)]$ is inferred from the field of damage driving force $Y[d(\vec{x}, t)]$ computed in a retrospective manner. If damage grows locally at $(\vec{x}_0, t_i)$, we assign $Y_{\mathrm{c}}[d(\vec{x}_0), t_i] = Y[d(\vec{x}_0), t_i]$ as well as for the preceding time steps (t_{i-}). We find that the average damage resistance $Y_{\mathrm{c}\circ}(d_\circ)$ increases with the damage level $d_\circ$. A linear approximation of the hardening behavior $Y_{\mathrm{c}\circ}(d_\circ) \sim \eta d_\circ$ with a hardening coefficient $\eta \simeq 45$ provides a good description of our experimental data upto failure.

5. Onset of damage localization

We provide here the methodology employed to determine the localization threshold. The basic idea is to compute the field of incremental damage growth at different distances to peak load as shown in Fig. 9(a) to determine whether it is homogeneous or localized. The incremental damage field $\delta d(\vec{x}) = d(\vec{x}, \delta) - d(\vec{x}, \delta + \epsilon)$ where $\epsilon \ll \delta$ is shown for three different values of δ: right before peak load ($\delta = 0.02$), at peak load ($\delta = 0$), and right after ($\delta = -0.02$). We clearly see the localization of the damage growth in a thin band for $\delta = -0.02$ from which we infer that the localization starts at peak load. The standard deviation $\sigma_{\delta d}(x) = \sqrt{\langle(\delta d(x) - \langle \delta d(\vec{x})\rangle_y)^2\rangle_y}$

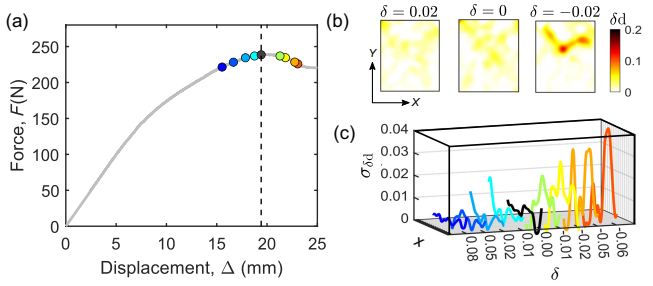

FIG. 9. The incremental damage field $\delta d(\vec{x})$ is computed for several locations δ near peak load as indicated by solid circles on the force-displacement curve of panel (a). (b) $\delta d(\vec{x})$ is represented right before ($\delta = 0.02$), at peak ($\delta = 0$), and right after ($\delta = -0.02$). Note the localization of the damage activity in the third panel suggesting that localization took place at peak load. (c) This is further confirmed by the standard deviation $\sigma_{\delta d}(x)$ of the incremental damage field that is shown to increase for $\delta < 0$.

is shown in Fig. 9(c) for several values of δ. Here also, we see that $\sigma_{\delta d}(x)$ increases above 0.01, suggesting that localization takes place at peak load.

APPENDIX B: NUMERICAL MODELING OF INTERMITTENT DAMAGE EVOLUTION AND LOCALIZATION

To solve the damage evolution equation under quasistatic loading conditions, we adopt the procedure described by Berthier *et al.* [45]. We consider a grid of size $L = 21$ discretized into L^2 elements with periodic boundary conditions. The interaction kernel is derived for the case of uniaxial compression using the method described by Dansereau *et al.* [58] and writes as

$$\psi(d_\circ) = \left[\frac{E'(d_\circ)^2}{E(d_\circ)^3}\right](1-\nu^2)\sigma_\circ^2\left[\frac{x^4 - 3y^4 + 6x^2y^2}{4\pi(x^2+y^2)^3}\right]. \quad \text{(B1)}$$

Interestingly, the kernel is independent of the type of loading configuration (stress vs strain imposed loading conditions). The amplitude of the kernel is also nonstationary, in contrast with the nonpositive interaction used to describe amorphous plasticity [61,62]. The variations of the elastic constant with the damage level is found to follow $E_\circ = E^\circ(1-d_\circ)^2$ with $E^\circ = 1.0$ MPa. We consider a heterogeneous field of damage resistance $Y_c[d(\vec{x},t)]$ that evolves with the damage level $d(\vec{x},t)$ following the linear hardening law $Y_{c\circ} = Y_c^\circ(1+\eta d_\circ)$, where $Y_c^\circ \simeq 1.4$ kJ/m^3 and $\eta \simeq 45$ are measured experimentally. The stress (strain) is gradually increased until the damage criterion is fulfilled for one of the elements $\vec{x} = \vec{x}_0$. The damage is increased locally, and the values of driving force $Y(\vec{x}_0,t)$ and resistance $Y_c(\vec{x}_0)$ are updated. The nonlocal redistribution of the driving force given by the kernel $\psi(d_\circ)$ may then trigger a cascade of damage events. The cascade stops when all elements are stable, following which, we increase the stress (strain) again.

The reader is invited to refer to the Supplemental Material [46] for a thorough description of the local analyses of experimental precursors, the theoretical and numerical modeling of damage accumulation, and the analogy with driven disordered elastic interface.

[1] J. Koivisto, M. Ovaska, A. Miksic, L. Laurson, and M. J. Alava, *Predicting sample lifetimes in creep fracture of heterogeneous materials*, Phys. Rev. E **94**, 023002 (2016).

[2] V. Kádár, G. Pál, and F. Kun, *Record statistics of bursts signals the onset of acceleration towards failure*, Sci. Rep. **10**, 1 (2020).

[3] S. Biswas, D. Fernandez Castellanos, and M. Zaiser, *Prediction of creep failure time using machine learning*, Sci. Rep. **10**, 1 (2020).

[4] W. Debski, S. Pradhan, and A. Hansen, *Criterion for imminent failure during loading—discrete element method analysis*, Front. Phys. **9**, 223 (2021).

[5] M. Ashby and C. Sammis, *The damage mechanics of brittle solids in compression*, Pure Appl. Geophys. **133**, 489 (1990).

[6] D. Lockner, J. Byerlee, V. Kuksenko, A. Ponomarev, and A. Sidorin, *Quasi-static fault growth and shear fracture energy in granite*, Nature (London) **350**, 39 (1991).

[7] M. Kachanov, *Elastic solids with many cracks: A simple method of analysis*, Int. J. Solids Struct. **23**, 23 (1987).

[8] J. Mazars and G. Pijaudier-Cabot, *Continuum damage theory—application to concrete*, J. Eng. Mech. **115**, 345 (1989).

[9] M. Kachanov, *Elastic solids with many cracks and related problems*, Adv. Appl. Mech. **30**, 259 (1993).

[10] J. Fortin, S. Stanchits, G. Dresen, and Y. Guéguen, *Acoustic emission and velocities associated with the formation of compaction bands in sandstone*, J. Geophys. Res. Solid Earth **111**, B10203 (2006).

[11] J. Fortin, S. Stanchits, G. Dresen, and Y. Gueguen, *Acoustic emissions monitoring during inelastic deformation of porous sandstone: Comparison of three modes of deformation*, Pure Appl. Geophys. **166**, 823 (2009).

[12] C. Manzato, A. Shekhawat, P. K. V. V. Nukala, M. J. Alava, J. P. Sethna, and S. Zapperi, *Fracture strength of disordered media: Universality, interactions, and tail asymptotics*, Phys. Rev. Lett. **108**, 065504 (2012).

[13] C. Manzato, M. J. Alava, and S. Zapperi, *Damage accumulation in quasibrittle fracture*, Phys. Rev. E **90**, 012408 (2014).

[14] Y. Tal, B. Evans, and U. Mok, *Direct observations of damage during unconfined brittle failure of Carrara marble*, J. Geophys. Res. Solid Earth **121**, 1584 (2016).

[15] P. Thilakarathna, K. K. Baduge, P. Mendis, V. Vimonsatit, and H. Lee, *Mesoscale modelling of concrete—a review of geometry generation, placing algorithms, constitutive relations and applications*, Eng. Fract. Mech. **231**, 106974 (2020).

[16] J. W. Rudnicki and J. Rice, *Conditions for the localization of deformation in pressure-sensitive dilatant materials*, J. Mech. Phys. Solids **23**, 371 (1975).

[17] W. A. Olsson, *Theoretical and experimental investigation of compaction bands in porous rock*, J. Geophys. Res. Solid Earth **104**, 7219 (1999).

[18] D. Lockner, *The role of acoustic emission in the study of rock fracture*, Int. J. Rock Mech. Min. Sci. Geomech. Abstr. **30**, 883 (1992).

[19] A. Petri, G. Paparo, A. Vespignani, A. Alippi, and M. Costantini, *Experimental evidence for critical dynamics in microfracturing processes*, Phys. Rev. Lett. **73**, 3423 (1994).

[20] S. Deschanel, L. Vanel, G. Vigier, N. Godin, and S. Ciliberto, *Statistical properties of microcracking in polyurethane foams under tensile test, influence of temperature and sensity*, Int. J. Fract. **140**, 87 (2006).

[21] J. Davidsen, S. Stanchits, and G. Dresen, *Scaling and universality in rock fracture*, Phys. Rev. Lett. **98**, 125502 (2007).

[22] J. Rosti, X. Illa, J. Koivisto, and M. J. Alava, *Crackling noise and its dynamics in fracture of disordered media*, J. Phys. D **42**, 214013 (2009).
[23] J. Baró, Á. Corral, X. Illa, A. Planes, E. K. H. Salje, W. Schranz, D. E. Soto-Parra, and E. Vives, *Statistical similarity between the compression of a porous material and earthquakes*, Phys. Rev. Lett. **110**, 088702 (2013).
[24] P. Castillo-Villa, J. Baro, A. Planes, E. K. H. Salje, P. Sellappan, W. M. Kriven, and E. Vives, *Crackling noise during failure of alumina under compression: The effect of porosity*, J. Phys. Condens. Matter **25**, 292202 (2013).
[25] J. Baró, K. A. Dahmen, J. Davidsen, A. Planes, P. O. Castillo, G. F. Nataf, E. K. H. Salje, and E. Vives, *Experimental evidence of accelerated seismic release without critical failure in acoustic emissions of compressed nanoporous materials*, Phys. Rev. Lett. **120**, 245501 (2018).
[26] C.-C. Vu, D. Amitrano, O. Plé, and J. Weiss, *Compressive failure as a critical transition: Experimental evidence and mapping onto the universality class of depinning*, Phys. Rev. Lett. **122**, 015502 (2019).
[27] D. Sornette, *Sweeping of an instability: An alternative to self-organized criticality to get power laws without parameter tuning*, J. Phys. I (France) **4**, 209 (1994).
[28] S. Zapperi, P. Ray, H. E. Stanley, and A. Vespignani, *First-order transition in the breakdown of disordered media*, Phys. Rev. Lett. **78**, 1408 (1997).
[29] S. Zapperi, A. Vespignani, and H. E. Stanley, *Plasticity and avalanche behaviour in microfracturing phenomena*, Nature (London) **388**, 658 (1997).
[30] D. Sornette, *Predictability of catastrophic events: material rupture, earthquakes, turbulence, financial crashes, and human birth*, Proc. Natl. Acad. Sci. U.S.A. **99**, 2522 (2002).
[31] H. Borja da Rocha and L. Truskinovsky, *Rigidity-controlled crossover: From spinodal to critical failure*, Phys. Rev. Lett. **124**, 015501 (2020).
[32] A. Guarino, A. Garcimartin, and S. Ciliberto, *An experimental test of the critical behaviour of fracture precursors*, Eur. Phys. J. B **6**, 13 (1998).
[33] L. Girard, D. Amitrano, and J. Weiss, *Failure as a critical phenomenon in a progressive damage model*, J. Stat. Mech. (2010) P01013.
[34] F. Kun, I. Varga, S. Lennartz-Sassinek, and I. G. Main, *Rupture cascades in a discrete element model of a porous sedimentary rock*, Phys. Rev. Lett. **112**, 065501 (2014).
[35] N. Kandula, B. Cordonnier, E. Boller, J. Weiss, D. K. Dysthe, and F. Renard, *Dynamics of microscale precursors during brittle compressive failure in Carrara marble*, J. Geophys. Res. Solid Earth **124**, 6121 (2019).
[36] S. Roux, A. Hansen, H. Herrmann, and E. Guyon, *Rupture of heterogeneous media in the limit of infinite disorder*, J. Stat. Phys. **52**, 237 (1988).
[37] A. Delaplace, G. Pijaudier-Cabot, and S. Roux, *Progressive damage in discrete models and consequences on continuum modelling*, J. Mech. Phys. Solids **44**, 99 (1996).
[38] A. Garcimartin, A. Guarino, L. Bellon, and S. Ciliberto, *Statistical properties of fracture precursors*, Phys. Rev. Lett. **79**, 3202 (1997).
[39] Y. Moreno, J. B. Gòmez, and A. F. Pacheco, *Fracture and second-order phase transitions*, Phys. Rev. Lett. **85**, 2865 (2000).
[40] J. Weiss, L. Girard, F. Gimbert, D. Amitrano, and D. Vandembroucq, *(Finite) statistical size effects on compressive strength*, Proc. Natl. Acad. Sci. U.S.A. **111**, 6231 (2014).
[41] F. Renard, J. Weiss, J. Mathiesen, Y. Ben-Zion, N. Kandula, and B. Cordonnier, *Critical evolution of damage toward system-size failure in crystalline rock*, J. Geophys. Res. Solid Earth **123**, 1969 (2018).
[42] A. L. Barabási and H. E. Stanley, *Fractal Concepts in Surface Growth* (Cambridge University Press, Cambridge, England, 1995).
[43] J. Sethna, K. Dahmen, and C. R. Myers, *Crackling noise*, Nature (London) **410**, 242 (2001).
[44] K. J. Wiese, *Theory and experiments for disordered elastic manifolds, depinning, avalanches, and sandpiles*, Rep. Prog. Phys. **85**, 086502 (2022).
[45] E. Berthier, A. Mayya, and L. Ponson, *Damage spreading in quasi-brittle disordered solids: II. What the statistics of precursors teach us about compressive failure*, J. Mech. Phys. Solids **162**, 104826 (2022).
[46] See Supplemental Material at http://link.aps.org/supplemental/10.1103/PhysRevX.13.041014 for details on the local analyses of experimental precursors, the theoretical and numerical modeling of damage accumulation.
[47] C. Poirier, M. Ammi, D. Bideau, and J. P. Troadec, *Experimental study of the geometrical effects in the localization of deformation*, Phys. Rev. Lett. **68**, 216 (1992).
[48] K. Karimi, D. Amitrano, and J. Weiss, *From plastic flow to brittle fracture: Role of microscopic friction in amorphous solids*, Phys. Rev. E **100**, 012908 (2019).
[49] F. Renard, J. McBeck, N. Kandula, B. Cordonnier, P. Meakin, and Y. Ben-Zion, *Volumetric and shear processes in crystalline rock approaching faulting*, Proc. Natl. Acad. Sci. U.S.A. **116**, 16234 (2019).
[50] A. Cartwright-Taylor, I. G. Main, I. B. Butler, F. Fusseis, M. Flynn, and A. King, *Catastrophic failure: How and when? Insights from 4-D in situ x-ray microtomography*, J. Geophys. Res. Solid Earth **125**, e2020JB019642 (2020).
[51] S. Lennartz-Sassinek, I. G. Main, M. Zaiser, and C. C. Graham, *Acceleration and localization of subcritical crack growth in a natural composite material*, Phys. Rev. E **90**, 052401 (2014).
[52] J. Davidsen, G. Kwiatek, E.-M. Charalampidou, T. Goebel, S. Stanchits, M. Rück, and G. Dresen, *Triggering processes in rock fracture*, Phys. Rev. Lett. **119**, 068501 (2017).
[53] P. Baud, E. Klein, and T.-f. Wong, *Compaction localization in porous sandstones: Spatial evolution of damage and acoustic emission activity*, J. Struct. Geol. **26**, 603 (2004).
[54] N. Lenoir, M. Bornert, J. Desrues, P. Bésuelle, and G. Viggiani, *Volumetric digital image correlation applied to x-ray microtomography images from triaxial compression tests on argillaceous rock*, Strain **43**, 193 (2007).
[55] J. A. McBeck, J. M. Aiken, J. Mathiesen, Y. Ben-Zion, and F. Renard, *Deformation precursors to catastrophic failure in rocks*, Geophys. Res. Lett. **47**, e2020GL090255 (2020).
[56] N. Kandula, J. McBeck, B. Cordonnier, J. Weiss, D. K. Dysthe, and F. Renard, *Synchrotron 4D x-ray imaging reveals strain localization at the onset of system-size failure*

in porous reservoir rocks, Pure Appl. Geophys. **179**, 325 (2022).

[57] E. Berthier, V. Démery, and L. Ponson, *Damage spreading in quasi-brittle disordered solids: I. Localization and failure*, J. Mech. Phys. Solids **102**, 101 (2017).

[58] V. Dansereau, V. Démery, E. Berthier, J. Weiss, and L. Ponson, *Collective damage growth controls fault orientation in quasibrittle compressive failure*, Phys. Rev. Lett. **122**, 085501 (2019).

[59] H. Hentschel and I. Procaccia, *The infinite number of generalized dimensions of fractals and strange attractors*, Physica (Amsterdam) **8D**, 435 (1983).

[60] D. Amitrano, *Variability in the power-law distributions of rupture events*, Eur. Phys. J. Special Topics **205**, 199 (2012).

[61] J. Lin, E. Lerner, A. Rosso, and M. Wyart, *Scaling description of the yielding transition in soft amorphous solids at zero temperature*, Proc. Natl. Acad. Sci. U.S.A. **111**, 14382 (2014).

[62] J. Lin, T. Gueudré, A. Rosso, and M. Wyart, *Criticality in the approach to failure in amorphous solids*, Phys. Rev. Lett. **115**, 168001 (2015).

[63] B. Lawn, *Fracture of Brittle Solids* (Cambridge University Press, Cambridge, England, 1993).

[64] E. Berthier, *Quasi-brittle failure of heterogeneous materials: Damage statistics and localization*, Ph.D. thesis, Université Pierre et Marie Curie, 2015.

[65] J. Lin and M. Wyart, *Mean-field description of plastic flow in amorphous solids*, Phys. Rev. X **6**, 011005 (2016).

[66] C. Liu, E. E. Ferrero, F. Puosi, J.-L. Barrat, and K. Martens, *Driving rate dependence of avalanche statistics and shapes at the yielding transition*, Phys. Rev. Lett. **116**, 065501 (2016).

[67] Z. Budrikis, D. F. Castellanos, S. Sandfeld, M. Zaiser, and S. Zapperi, *Universal features of amorphous plasticity*, Nat. Commun. **8**, 1 (2017).

[68] M. Ozawa, L. Berthier, G. Biroli, A. Rosso, and G. Tarjus, *Random critical point separates brittle and ductile yielding transitions in amorphous materials*, Proc. Natl. Acad. Sci. U.S.A., **115**, 6656 (2018).

[69] J.-C. Anifrani, C. Le Floc'h, D. Sornette, and B. Souillard, *Universal log-periodic correction to renormalization group scaling for rupture stress prediction from acoustic emissions*, J. Phys. I (France) **5**, 631 (1995).

[70] A. Mayya, E. Berthier, and L. Ponson, *Procédé et dispositif d'analyse d'une structure*, French Patent Application No. FR2002824 (2020).

[71] G. F. Nataf, P. O. Castillo-Villa, J. Baró, X. Illa, E. Vives, A. Planes, and E. K. H. Salje, *Avalanches in compressed porous SiO_2-based materials*, Phys. Rev. E **90**, 022405 (2014).

[72] J. Davidsen, T. Goebel, G. Kwiatek, S. Stanchits, J. Baró, and G. Dresen, *What controls the presence and characteristics of aftershocks in rock fracture in the lab?*, J. Geophys. Res. Solid Earth **126**, e2021JB022539 (2021).

[73] Y. Xu, A. G. Borrego, A. Planes, X. Ding, and E. Vives, *Criticality in failure under compression: acoustic emission study of coal and charcoal with different microstructures*, Phys. Rev. E **99**, 033001 (2019).

[74] N. Zreihan, E. Faran, E. Vives, A. Planes, and D. Shilo, *Relations between stress drops and acoustic emission measured during mechanical loading*, Phys. Rev. Mater. **3**, 043603 (2019).

[75] G. Parisi, I. Procaccia, C. Rainone, and M. Singh, *Shear bands as manifestation of a criticality in yielding amorphous solids*, Proc. Natl. Acad. Sci. U.S.A. **114**, 5577 (2017).

[76] J. Schindelin, I. Arganda-Carreras, E. Frise, V. Kaynig, M. Longair, T. Pietzsch, S. Preibisch, C. Rueden, S. Saalfeld, B. Schmid *et al.*, *fiji: An open-source platform for biological-image analysis*, Nat. Methods **9**, 676 (2012).

[77] M. A. Lebyodkin, I. V. Shashkov, T. A. Lebedkina, K. Mathis, P. Dobron, and F. Chmelik, *Role of superposition of dislocation avalanches in the statistics of acoustic emission during plastic deformation*, Phys. Rev. E **88**, 042402 (2013).

[78] D. Houdoux, T. B. Nguyen, A. Amon, and J. Crassous, *Plastic flow and localization in an amorphous material: Experimental interpretation of the fluidity*, Phys. Rev. E **98**, 022905 (2018).

[79] D. Houdoux, A. Amon, D. Marsan, J. Weiss, and J. Crassous, *Micro-slips in an experimental granular shear band replicate the spatiotemporal characteristics of natural earthquakes*, Commun. Earth Environ. **2**, 90 (2021).

[80] B. Glasser and I. Goldhirsch, *Scale dependence, correlations, and fluctuations of stresses in rapid granular flows*, Phys. Fluids **13**, 407 (2001).